FISEVIER

Contents lists available at ScienceDirect

# **Additive Manufacturing**

journal homepage: www.elsevier.com/locate/addma



# Research paper



# Non-isothermal non-Newtonian three-dimensional flow simulation of fused filament fabrication

Sun Kyoung Kim<sup>a,\*</sup>, David O. Kazmer<sup>b,\*</sup>

- a Seoul National University of Science and Technology, Department of Mechanical System Design Engineering, Seoul 01811, Republic of Korea
- b Department of Plastics Engineering, University of Massachusetts Lowell, Lowell, MA 01854, USA

#### ARTICLE INFO

#### Keywords: Viscosity Material extrusion Simulation Additive manufacturing Modeling

#### ABSTRACT

This work investigates three-dimensional simulation of fused filament fabrication using the Cross-WLF model for the non-isothermal and shear thinning behavior of the melt. To realistically simulate the deposition flow, the acceleration, viscosity evolution, and flow front tracking models have been included with the pressure gradient in the deposited road and boundary modeling of the melt and air interface. The results indicate that the non-isothermal and shear thinning behaviors greatly affect the geometry of the deposited roads including the flow front and trailing cross-section shapes. The thermal footprint of the interface between the deposited melt and the substrate is also predicted as a function of the thermal contact conductance. The pressure distribution within the deposited road is also modeled and is found to be not symmetric with respect to the nozzle center-line. Rather, the pressure peak shifts slightly downstream due to redirection of the melt around a stagnation point opposite the nozzle exit. Furthermore, a negative stress is observed downstream the exterior nozzle face associated with the free expansion of the melt as the extruded material climbs and releases from the exterior nozzle face. The developed simulation is verified by comparison with experimental results providing contact pressures ranging from 5 to 132 kPa.

# 1. Introduction

Additive manufacturing by material extrusion, also referred to as fused filament fabrication (FFF), became one of the popular three-dimensional printing processes since it allows building complex structures in a versatile and cost-efficient way without tooling [1]. In a typical process, wound thermoplastic filament is fed from a reel through an extruder's drive gears to a hot end. The rotation of the drive gears is controlled to deliver the processed filament to the nozzle at a controlled linear velocity. Moving through the hot end, the filament is heated to above the set temperature by heat conduction within the hot end wall. Near the nozzle exit, the feedstock is fully plasticated as thermoplastic melt with a processible viscosity. Then, the melt is extruded out of the nozzle by the feed action forming an interface with surrounding air. Afterwards, the melt contacts and remains deposited on the build plate and previously printed substrate that is moving at a controlled speed relative to the nozzle.

The dynamic flow near and downstream of the nozzle exit is of specific interest since it will affect the deposition process, subsequent weld healing, and final properties of the built structure. The melt

experiences dramatic changes both thermally and rheologically. Thus, the simulation of this process has become a matter of great importance. As is in other thermoplastic processes, the simulation of the material extrusion additive manufacturing entails several difficulties. First of all, the rheological properties of the melt are not easy to treat during the numerical simulation. Second, the free boundary should be tracked during the process. Third, the process involves a solidification process while cooling. Thus, implementation of all these is not trivial by simulation even with modern computational resources.

There have been some studies on modeling [2,3] but rather few studies have investigated numerical simulations of flow and subsequent cooling. Earlier in 2002, Bellini simulated the non-isothermal deposition flow using a deforming axisymmetric geometry with the power law model [4]. Ramanath et al. solved the melt flow inside a curved nozzle using Ansys Flotran [5]. Their work was interested in determination of the fully molten location. Later in 2018, Xia et al. presented a method that solves deposition and cooling using a finite difference code based on the fractional step method. That work neglected the details of the melt flow near the nozzle and focused on the deposition followed by cooling [6]. Then, they extended their study to consider viscoelasticity of the

E-mail addresses: sunkkim@seoultech.ac.kr (S.K. Kim), David\_Kazmer@uml.edu (D.O. Kazmer).

<sup>\*</sup> Corresponding authors.

filament melt [7]. Comminal et al. has solved the nozzle exit flow with the isothermal and Newtonian assumptions using Ansys Fluent 15. They have shown plausible flow fronts and conceptually useful process windows [8]. Agassant et al. have also solved the flow out of the nozzle also with isothermal and Newtonian approximations using the CIMLIB library, which is renowned for application in twin screw simulations. Their work has obtained approximate pressure field and flow front shape near the nozzle [9]. They have compared the numerical results of the pressure and the road width with those by their analytical model. Behdani et al. simulated a non-isothermal deposited flow based on the power law model with OpenFOAM and showed cross-sections of the strand [10]. Gosset et al. also used OpenFOAM to solve an isothermal three-dimensional flow [11]. They compared the obtained cross-section with the experimental result. More recently, Phan et al. presented simulation results for melting inside the nozzle and extrusion flows [12].

Our research is motivated by the need to more accurately simulate the non-isothermal flow in the region between the nozzle and the substrate, thereby providing guidance as to product quality modeling as well as further machine, process, and material engineering. The simulation models the experimental setup described in previous works [13–15]. The Cross-WLF model will implement the rheological properties of the filament as realistically as possible. To provide the temperature to the viscosity model and to visualize the cooling process, the energy equation will be solved. In addition to this non-isothermal feature, this work will solve viscous non-Newtonian flow to accommodate the shear thinning occurring during the printing process. Compressibility would have a measurable effect on the output flow and shape of the deposited road in the presence of a steep pressure gradient. However, experimental characterization of the contact pressure [14,15] show that the pressures within the deposited road are very low (typically less than 0.1 MPa) and so compressibility will not have a significant effect on the shape of the extrudate. Elasticity is a different matter since the strain fields vary with changes in cross-section of the melt and can have a significant effect with predicted die swell behaviors varying greatly between models [16,17]. However, the rate of radial velocity change of the melt out of the nozzle is small given that deposited roads are typically on the same order of magnitude as the nozzle diameter. While two-dimensional analyses of viscoelastic flows seem viable [16, 18], a full three-dimensional one is unlikely to provide a solution within a reasonable computational time. As such, this work focuses on the temperature dependence and shear thinning behaviors with the intent to provide predictive accuracy of the melt pressure.

In this work, to accurately model the shape of the flow front, the level set method is employed. This work has selected COMSOL 5.6 (Comsol

Inc, Burlington, MA, USA) for implementation since it allows flexibility in multi-physics and material constitutive modeling, which are inevitably necessary to realize this demanding simulation. As such, this paper provides full disclosure of the details including reference models in the supplementary materials. Given the importance of transient effects, the startup flow of the material extrusion and deposition has been solved and presented to show the development. This work will also argue the necessity of the non-isothermal simulation and its rheological implications. Moreover, the pressure development and resulting contact pressure during the printing process has been characterized based on the simulation results [19].

#### 2. Numerical method

#### 2.1. Process model

Consider a material extrusion and deposition model as shown in Fig. 1. The hot end and nozzle assembly dispenses molten filament onto build plate or substrate moving at a relative transverse velocity. In actual material extrusion processes, the direction of printing varies in magnitude and direction with time, but the current model assumes a linear motion in the x-direction. The nozzle center line is considered along the z-axis and perpendicular to the build plate. The nozzle's bottom surface is parallel with the build plate as shown in Fig. 1. The melt flows into the domain at a flow rate that is supposed to be controlled at a constant value. However, the flow starts from an initial state of zero flow rate such that it requires a transient interval. Thus, the flow rate is denoted as Q(t), and likewise, the print speed, S(t), is also a function of time.

To analyze the flow of interest, a control volume is set including the internal flow within the nozzle bore as well as the external flow between the nozzle wall and the build plate or substrate as shown in Fig. 1. The internal flow upstream of the nozzle bore is excluded in the analysis, currently assuming a pressurized reservoir of uniform fluid at the inlet temperature; this assumption is of current interest and interested readers are directed to other literature [12,19]. If a moving nozzle is considered as in an actual process, the control volume should move as if attached to the nozzle. However, a fixed nozzle with a moving built plate is assumed since a moving control volume can incur difficulties in modeling and simulation as in many moving body flow simulations.

#### 2.2. Numerical scheme

This work aims at numerically simulating a startup flow of material extrusion and deposition of a non-Newtonian thermoplastic melt under

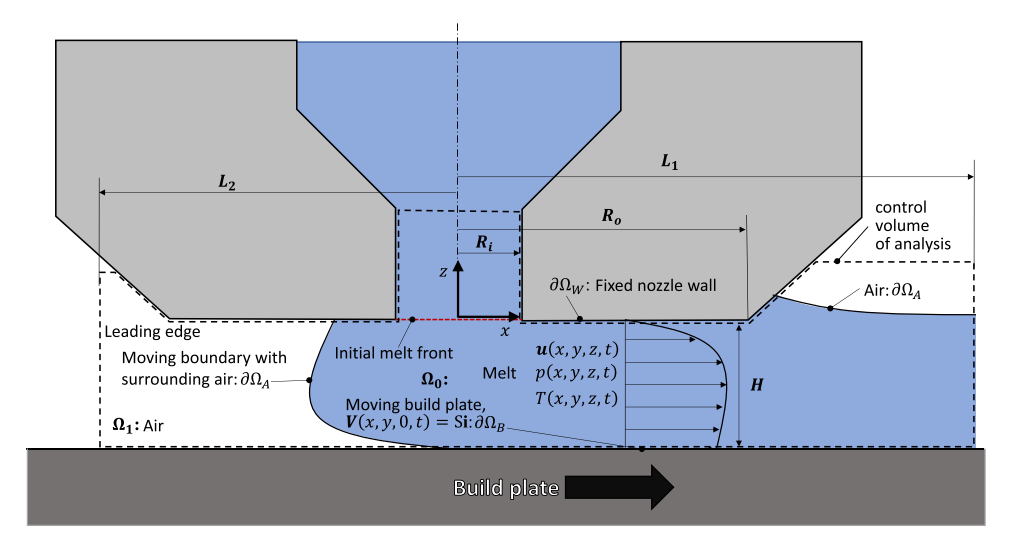


Fig. 1. Overview of process & modeled computational domain

non-isothermal condition. The simulation scheme entails PDE (partial differential equation) models including the momentum equation of a GNF (generalized Newtonian fluid) and the non-isothermal energy equation as well as several algebraic models. The flow front is initialized as a circular disc at the exit of the nozzle and then modeled as a quasispherical, free flow outwards and towards the build plate as shown in Fig. 1. The flow front development in the vicinity of the nozzle is of great interest. Moreover, the pressure development here can dramatically affect the mechanical quality of the bonding between the layers [15]. Thus, the flow front should be captured accurately and is tracked by solving the level set equation. These three equations (momentum, energy, and level set) subject to the corresponding BCs (boundary conditions) are solved in conjunction with the Cross-WLF viscosity, process startup and evolution models according to the solution methodology depicted in Fig. 2. All the aforementioned components are implemented in COMSOL 5.6. As a result of the numerical analysis, the velocity, V, pressure, p, temperature T and the moving boundary between air and melt, as shown in Fig. 1, will be achieved as a function of time and space. In the subsequently described work, the domain and the boundary are as denoted in Fig. 1.

#### 2.3. Governing equation

For incompressible fluids, the continuity equation is given by

$$\rho \nabla \cdot \mathbf{u} = 0 \tag{1}$$

where  ${\bf u}$  and  $\rho$  are the velocity vector and the density, respectively. Neglecting the body force and the surface tension, the momentum equation is expressed as

$$\rho \frac{\partial \mathbf{u}}{\partial t} + \rho \left( \mathbf{u} \cdot \nabla \right) \mathbf{u} = \nabla \cdot [-p\mathbf{I} + \boldsymbol{\tau}]$$
 (2)

where p is the pressure and  $\tau$  is the deviatoric stress tensor, respectively. The force by the surface tension and the gravity is multiple orders of magnitude smaller than those by the pressure and the viscous shear

[11]. Thus, they are neglected to reduce the computational loads. The constitutive equation for a generalized Newtonian fluid with a viscosity of  $\eta$  is stated as

$$\tau = \eta \mathbf{D} \tag{3}$$

where D is the strain rate tensor represented by

$$\mathbf{D} = \nabla \mathbf{u} + \nabla \mathbf{u}^T \tag{4}$$

The square-root of half the second invariant of  ${\bf D}$  gives the magnitude of the strain rate tensor, which is written as

$$\dot{\gamma} = \left(\frac{\mathbf{D} : \mathbf{D}^T}{2}\right)^{0.5} \tag{5}$$

To obtain the temperature, *T*, the following energy equation has to be solved:

$$\rho C_p \left( \frac{\partial T}{\partial t} + \mathbf{u} \cdot \nabla T \right) = \nabla \cdot \left( k \nabla T \right) + \eta \dot{\gamma}^2 \tag{6}$$

where  $C_p$  and k are the specific heat capacity, thermal conductivity, respectively.

#### 2.4. Viscosity model

The dynamic viscosity is modeled as the Cross-WLF model to represent the non-Newtonian behavior of polymer melt. For a given temperature, T, the corresponding viscosity function  $\eta(\dot{\gamma},T)$  is of the form [20,21]:

$$\eta\left(\dot{\gamma},T\right) = \frac{\eta_0(T)}{1 + (\eta_0(T)\dot{\gamma}/\tau)^{1-n}}\tag{7}$$

where n is the index and  $\tau$  is a coefficient. In addition, the temperature dependence of the zero-shear viscosity is [22]:

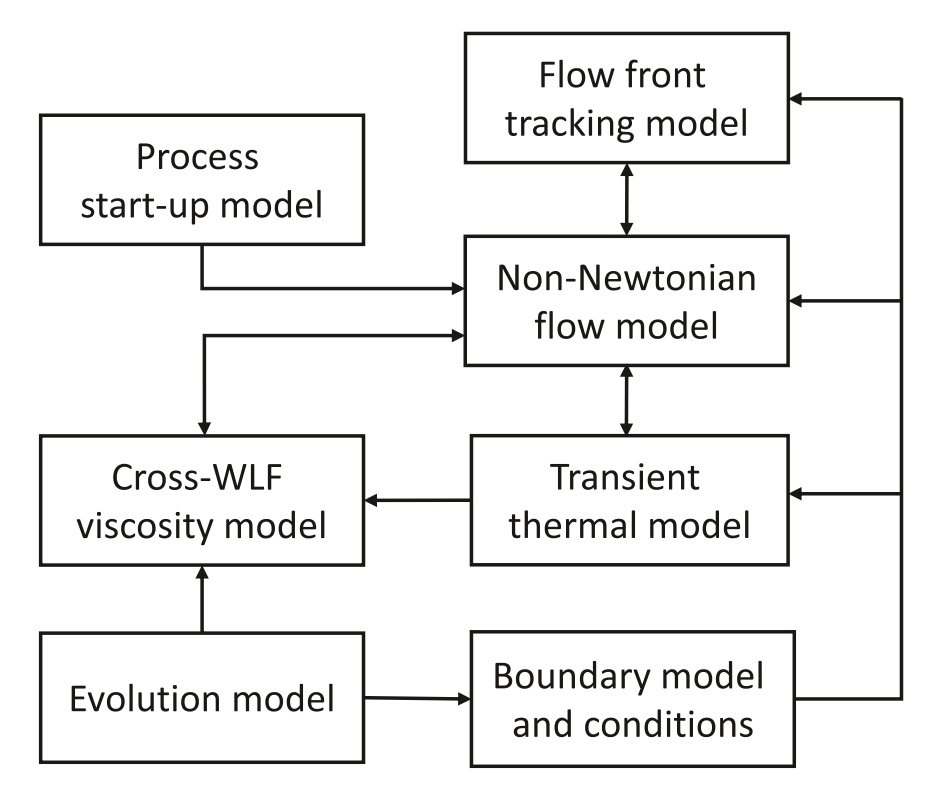


Fig. 2. Computational scheme of the numerical simulation.

$$\eta_0 = D_1 \exp\left[\frac{-A_1(T - D_2)}{A_2 + (T - D_2)}\right] for T \ge D_2$$
(8)

$$\eta_0 = D_1 for T \ge D_2 \tag{9}$$

where  $A_1$ ,  $A_2$ ,  $D_1$  and  $D_2$  are fitted model coefficients determined from experimental measurements for a specific polymer. This viscosity model is implemented with a user material model in COMSOL.

#### 2.5. Flow front tracking

To efficiently capture the flow front, the level set method has been chosen. The level set function,  $\nabla$ , renders smooth transition from 0 to 1 with the interface  $\partial\Omega_{\rm A}$  on  $\varphi=0.5$ . In this work, the surrounding air and the polymer phases are represented by  $\varphi=0$  and  $\varphi=1$ , respectively. In the interface region,  $0<\varphi<1$ , the material property is given by the rule of mixture. For example, the viscosity there is set as  $\eta_{\varphi}=\mu_{air}+\varphi(\eta-\mu_{air})$  where  $\mu_{air}$  is the viscosity of air.

Traditionally, the level set method solves an advection problem defined by  $\frac{\partial \varphi}{\partial t} + u \cdot \nabla \varphi = 0$  [23]. A discretized form of this equation is subjected to numerical diffusion resulting in smeared interfaces. To maintain the resolution of the interfaces, the numerical diffusion needs to be suppressed by the reinitialization procedure. This has been achieved by the artificial compression subproblem defined by  $\frac{\partial \varphi}{\partial \tau} + \nabla \cdot \left[ \varphi(1-\varphi) \frac{\nabla \varphi}{|\nabla \varphi|} \right] = \Gamma \nabla^2 \varphi$  where  $\tau$  is the artificial time and  $\Gamma$  is the compression parameter [24,25]. Consequently, an intermediate step is required to determine the interface at each time step. To avoid the intermediate step, by introducing the interface thickness,  $\varepsilon$ , and replacing  $\Gamma$  with the compression velocity,  $\gamma$ , those two equations are merged to [25–27].

$$\frac{\partial \varphi}{\partial t} + \mathbf{u} \cdot \nabla \varphi = \gamma \nabla \cdot \left[ \varepsilon \nabla \varphi - \varphi \left( 1 - \varphi \right) \frac{\nabla \varphi}{|\nabla \varphi|} \right]$$
(10)

To accurately render the interface,  $\gamma$  needs to be suitably tuned around the maximum of  $\|u\|$  by trial and error while  $\varepsilon$  has to be set depending on the mesh size around the free surface.

# 2.6. Geometric setup

The geometry of this simulation contains a higher mesh density region where the melt flow develops. The roughly cuboid domain is shown in Fig. 3, which realizes the control volume in Fig. 1. The detail of the nozzle exit region is implemented in utilizing a half-symmetry with respect to the x-z plane. Refer to Fig. 3 for definition of the geometric parameters including H,  $H_1$ ,  $H_2$ ,  $L_1$ ,  $L_2$ ,  $R_i$ ,  $R_0$ ,  $W_1$  and  $\theta$ . Among them, H,

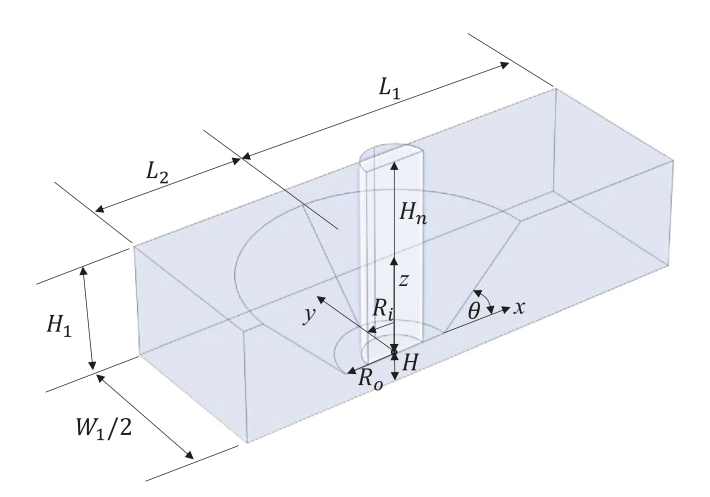


**Fig. 3.** Three-dimensional control volume of the numerical domain with geometric parameters.

 $R_i$ ,  $R_o$ , and  $\theta$  are determined according to the physical process design. To take the effect of internal flow development in the nozzle into account, sufficiently large  $H_n$  should be selected. The length of the downstream domain,  $L_1$ , should be long enough to model the stabilizing flow out of the nozzle vicinity. Other constants such as  $H_1$ ,  $L_2$  and  $W_1$ , should be large enough that the BCs representing the surrounding temperature and pressure can be imposed safely. Given the relative flow direction,  $L_2$  does not have to be as long as  $L_1$ . In this work,  $W_1/2$  is set slightly larger than  $R_o + (H_1 - H)\cot\theta$  since an increased domain or mesh density would increase the computational cost without significantly changing the results.

#### 2.7. Boundary conditions

Solutions of Eqs. (1), (2), (5) and (10) require boundary conditions on the control surface defined by the volume in Fig. 3. As aforementioned and shown in Fig. 1, the free boundary between the air and the melt is denoted as  $\partial\Omega_A$ . The initial  $\partial\Omega_A$  is in-plane with the nozzle outlet as shown in Fig. 1. This boundary moves and deforms along with the melt flow inside the domain shown in Fig. 3. In the meantime, six different kinds of external boundaries are involved in this numerical procedure. Refer to Fig. 1 and Fig. 4 for these boundaries. First, a symmetry condition should be imposed on  $\partial\Omega_S$  defined on y=0. A fixed wall boundary region,  $\partial\Omega_W$ , is defined by the inner and outer surface of the nozzle. The inner boundary of the nozzle is always wet with the melt, but the initially dry outer boundary can be dry or wet depending on the time and position. Moreover, a wall moving at a velocity of S in the x-direction is set on  $\partial\Omega_B$  as illustrated in Fig. 1 and Fig. 4.

In the FFF machine, Q(t), S(t) and H are controlled according to a process plan governing linear displacements. A fully-developed laminar inlet flow is imposed on  $\partial\Omega_{\rm I}$ , where a flow rate of Q/2 should be given considering the symmetry on  $\partial\Omega_{\rm S}$ . Assuming a rectilinear steady flow, a nominal road width can be evaluated by

$$W = \frac{Q(t)}{S(t)H} \tag{11}$$

Note that this width is only a target value and the actual printed road width will be determined as the road shape dynamically evolves.

On  $\partial\Omega_{\rm B}$  and  $\partial\Omega_{\rm W}$ , the temperatures are controlled respectively as the substrate or build plate temperature,  $T_{\rm B}$ , and the nozzle wall temperature,  $T_{\rm W}$ . Dirichlet thermal conditions can be imposed assuming perfect thermal contact between the melt and the wall. However, it is known that there exists thermal contact resistance (TCR) in such a situation despite the no slip condition in the flow [5]. In this work, the thermal contact conductance  $h_{\rm B}$  and  $h_{\rm W}$  are introduced to express the thermal boundary conditions, respectively on  $\partial\Omega_{\rm B}$  and  $\partial\Omega_{\rm W}$  as follows:

$$-k\frac{\partial T}{\partial n} = h_B[T - T_B] \text{ on } \partial\Omega_B$$
 (12)

$$-k\frac{\partial T}{\partial n} = h_W[T - T_W] \quad on \quad \partial \Omega_W$$
 (13)

where  $\partial T/\partial \mathbf{n} \equiv \nabla T \cdot \mathbf{n}$  for the surface unit normal vector,  $\mathbf{n}$  on the corresponding boundary. The thermal contact conductance (TCC), which is the reciprocal of TCR, takes the same form as the heat transfer coefficient, but the former, unlike the latter, represents the reciprocal of the temperature jump between the solid and the polymer walls for the heat flow through the boundary [28]. The TCC can drastically vary according to the properties of the build plate or the preceding deposited layers including the surface roughness, the thermal conductivity and the heat capacity. Moreover, the normal stress onto the build plate should influence the TCC.

Here, specification of  $h_B$  and  $h_W$  becomes a matter of interest since it greatly affects the temperature field in the healing zone of FFF. For comparison, in injection molding, the TCC between the melt and the mold wall typically ranges from 100 to 30,000 W/m<sup>2</sup>K [29–33]. This wide range can be attributed to the wettability of the polymer melt and

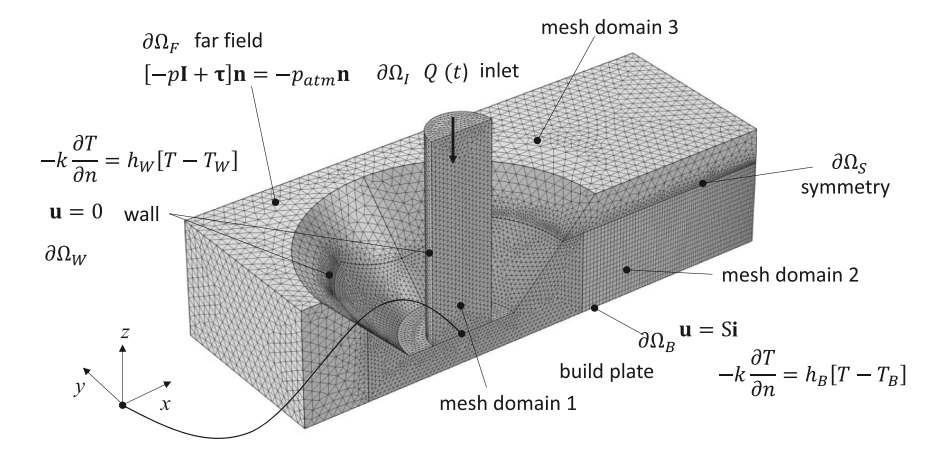


Fig. 4. Mesh with 1,514,513 elements and boundary conditions.

adjacent boundaries, surface roughness, and local melt pressures. For melt extrusion additive manufacturing processes, empirical data are currently not available and the pressure around the interface is comparatively low, so a value of  $100~\text{W/m}^2\text{K}$  is initially chosen and later investigated.

In the far field boundary of the outer domain denoted by  $\partial\Omega_{\rm F}$ ,  $[-p{\bf I}+{\bf \tau}]{\bf n}=-p_{am}{\bf n}$  is imposed to allow the open boundary. The three of the four faces on  $\partial\Omega_{\rm F}$  cannot be reached by the melt and thus is subject to a level set condition of  $\phi$  for improved numerical stability. The melt flows outward to the right end through the boundary at  $x=L_1$ , while the air can move in or out of the other boundaries.

#### 2.8. Acceleration

The inlet flow rate, Q, into the boundary  $\partial\Omega_I$  cannot be a step rise in real nozzles. As the initial velocity is considered zero over the whole domain, the inlet flow rate has to be accelerated from zero to the target value. Consider a proportional control of a start-up procedure toward a steady flow rate of  $Q_0$  taking the flow rate increase rate, dQ/dt, as a control variable. It is described by  $dQ/dt \propto Q_0 - Q$  and the flow rate is obtained as

$$Q(t) = Q_0 \left[ 1 - \exp\left(-\frac{t}{t_1}\right) \right] \tag{14}$$

where  $t_1$  is the time constant that has a physical meaning related to the acceleration of the filament in the hot end while also serving as a numerical stabilizer. Similarly, the movement of the build plate can be described as

$$S(t) = S_0 \left[ 1 - \exp\left(-\frac{t}{t_1}\right) \right] \tag{15}$$

Note that the same time constant  $t_1$  has been set to maintain  $Q(t)/Q_0 = S(t)/S_0$  to synchronize the extrusion with the build plate and thereby maintain Eq. (13) throughout the entire time. The time constant is set taking the maximum acceleration of the build plate into account. The maximum acceleration of a typical FFF machine is known to be 3 m/s² [34]. Since it takes 4.6 $t_1$  to reach 99% of the steady speed,  $t_1$  is set as  $S_0/13.8$ .

# 2.9. Viscosity evolution

The non-Newtonian viscosity induces a significant nonlinearity in the numerical method such that an iterative solution may fail in finding a proper path to a converging solution. The non-isothermal process further raises the convergence difficulty. The solution procedure in this work is comprised of two steps. In the first step, a Newtonian solution assuming

$$\eta_N = \eta \left( \frac{S}{H}, T_e \right) \tag{16}$$

where  $T_e$  is the initial estimate of the extrudate temperature defined by

$$T_e = \frac{T_W + T_B}{2} \tag{17}$$

is obtained. Then, the non-Newtonian solution is achieved by an evolution scheme by

$$\eta_{\theta} = \theta \eta(\dot{\gamma}, T) + (1 - \theta) \eta_{N} \tag{18}$$

where  $\gamma$  is a convergence parameter within each time step defined as a function of time t such that

$$\theta = \frac{p_1^2 t^2}{1 + p_1^2 t^2} \tag{19}$$

Similar schemes are found in [35,36]. Here, the evolution speed is controlled by the evolution parameter,  $p_1$ . With a large  $p_1$ , the numerical procedure may not smoothly start from the initial state and so can fail. However, larger values of  $p_1$  will favor more accurate viscosity estimations so it is necessary to select the largest possible value that allows convergence. Typical values of  $p_1$  are greater than ten times the reciprocal of the characteristic processing time so as to stabilize the solution process and at the same time reduce the error in the viscosity from the initial value.

#### 3. Results

#### 3.1. Simulation conditions

The FFF process conditions considered in the simulations are described here. The geometric constants in Fig. 3 are listed in Table 1. The filament material is a PS(polystyrene) used in the previous experimental works [14,15]. The specific constants for the viscosity model by Eq. (7-9) are specified in Table 2. The melt temperature,  $T_{\rm m}$ , and the

Table 1
The geometric parameters in Fig. 3.

Gap between nozzle bottom and build plate, ${\cal H}$	0.25 mm
Taper height, $H_1$	0.75 mm
Inlet height, $H_n$	1.72 mm
Nozzle bore radius, R <sub>o</sub>	0.475 mm
Nozzle face radius, R <sub>i</sub>	0.265 mm
Nozzle taper angle, $\theta$	45°
Trailing mesh length, $L_1$	2.8 mm
Leading mesh length, $L_2$	1.4 mm
Mesh width, $W_1$	3 mm
Inlet height, $H_n$ Nozzle bore radius, $R_o$ Nozzle face radius, $R_i$ Nozzle taper angle, $\theta$ Trailing mesh length, $L_1$ Leading mesh length, $L_2$	1.72 mm 0.475 mm 0.265 mm 45° 2.8 mm 1.4 mm

**Table 2**The Cross-WLF viscosity constants of the polystyrene melt [13].

$A_1$	19.8
A <sub>2</sub> D <sub>1</sub> τ *	51.6 K 4.91 × 10 <sup>9</sup> Pa•s 2.64 × 10 <sup>4</sup> Pa
τ * n T *	2.64 × 10 ° Pa 0.305 371 K

ambient temperature,  $T_{\rm atm}$ , are set as 250 °C and 20 °C, respectively. The plate temperature,  $T_B$ , is set 80 °C. The density of the PS melt at  $T_{\rm m}$  is 949.1 kg/m³ according to the relation in [37]. The speed of plate,  $S_0$ , is set as 2500 mm/min or 41.7 mm/s, with a flow rate,  $Q_0$  of 10.42 mm³/s unless specified. These conditions result in a mean nozzle exit velocity of 47.23 mm/s such that velocity ratio to  $S_0$  is 1.13. The temperature of the nozzle,  $T_{\rm w}$ , is assumed to be controlled at  $T_{\rm m}$ . The heat transfer coefficients  $h_{\rm w}$  and  $h_{\rm B}$  are each initially set to 100 W/m²K until later investigated. The compression velocity  $\gamma$  and the evolution parameter  $p_1$  are set as 0.001 and 2000 s $^{-1}$ , respectively.

#### 3.2. Numerical discretization and mesh

For the momentum equation, Eq. (2), the solution adopts the mini (P1 + P1) element with linear shape functions for both the velocity and pressure. Also, for the energy equation, Eq. (6), the linear element has been put into use. However, for the level set equation, Eq. (12), quadratic elements are employed to obtain sharper interfaces by suppressing the artificial diffusion [38]. In COMSOL, the solution procedure of Eq. (2) and Eq. (6) is stabilized by the streamline and crosswind diffusions [39,40]. Moreover, the time domain is discretized by an implicit Euler method, the BDF (backward differentiation formula). A variant of GMRES (generalized minimum residual) method gives the solution for each time step. The numerical time step is adaptively selected based on the tolerance, which is set as 0.01 here. For further information on the adaptive time step and the tolerance, refer to [41].

The melt experiences extreme changes in the direction and the external condition while exiting the nozzle and entering the region below the nozzle. Hence, this region requires a fine mesh. This inevitably renders the overall mesh density quite high. To achieve computational efficiency, the geometry is divided into three domains for meshing as shown in Fig. 4. The first domain is comprised of the internal flow regime inside the nozzle and the initial extruded flow. The second domain includes the downstream extrudate flow. Thus, all printed road regimes are typically contained in the first and second domains. The third domain is for the rest of the geometry typically comprised only of air. The first domain is uniformly discretized by automatically generated tetrahedral elements with a size between 0.03 and 0.04 mm to accurately capture the free surface. The second domain is discretized by prism elements in a similar scale by sweeping the boundary of the first domain along the x axis to share the surface nodes between the first and second domains. The third domain is relatively sparsely discretized by tetrahedral elements with a size up to 0.08 mm. When the mesh is automatically generated in the third domain, the connectivity is guaranteed since the elements are created using the existing nodes on the boundaries of the first and third domains. For the current mesh size, h, and the previous mesh size,  $h_p$ , the mesh convergence has been checked by  $\left\|p^h-p^{h_p}\right\|_2 \leq 10^{-4}\left\|p^{h_p}\right\|_2$  where the test pressures are sampled at 100different locations while mesh size is reduced by  $h = 0.9h_p$ . As a result, a mesh with 1,514,513 elements shown in Fig. 4 has been built.

#### 3.3. Comparison of thermo-rheological models

To investigate the effects of the different thermo-rheological models, the isothermal Newtonian, isothermal Cross, Newtonian-WLF and Cross-

WLF models are tested. Regarding the Newtonian viscosity, it has been imposed by Eq. (18) as similarly done in [9]. Fig. 5 shows shapes of printing flows and the downstream cross-sections at  $x = L_1$  for different material constitutive models; side views on the x-z symmetry plane are shown in Fig. 6. It is also noticeable in Fig. 6 that the flow climbs the trailing surface of the nozzle chamfer and then detaches. This behavior is attributed to the locally high pressures in the trailing deposited road that lead to a hydrodynamic jump past the constraining nozzle as characteristic to open channel flows. Despite the build plate movement, the pressure dominantly drives the flow below the nozzle (refer to Fig. S3 for the velocity profile). Regarding the shape of the initial flow front near the nozzle, the Newtonian assumption seems sufficient since all the three-dimensional rendered printing flow fronts in Fig. 5 appear similar. The leading flow front shapes also support the conclusion in [8] that an accurate value of the viscosity is not essential at a macroscopic level for modeling a controlled flow rate. However, the trailing cross-sections predicted by the isothermal Newtonian, isothermal Cross, Newtonian-WLF and Cross-WLF models are all very different from each other. The observed behaviors are as follows:

- The Newtonian model tends to have the most deformed flow including a pronounced hydrodynamic jump with the trailing flow front climbing the inclined outer surface of the nozzle. Furthermore, the Newtonian model has the most post-deposition flow with the trailing cross-section reverting to a semi-circle.
- The isothermal Cross model possesses many of these same behaviors albeit to a lesser extent. The reason is that the isothermal Cross model provides a higher viscosity at a lower  $\dot{\gamma}$  such that the bulk of the flow regime has less deformation than the Newtonian model. As a result, the isothermal Cross model predicts that the trailing edge does not climb the outer surface or roll-off as much as the Newtonian model.
- The Newtonian-WLF model is non-isothermal but does not include the shear dependent behavior of the viscosity. As the melt contacts the substrate, the deposited material begins to cool and the viscosity increases very quickly. However, the material above the cooling layers remains warm with a relatively low, shear-independent viscosity. As a result, an overhang is observed in the trailing cross-section of Fig. 5(c) as well as the trailing side view of Newtonian-WLF at 0.05 s in Fig. 6.
- The cross-section for the full Cross-WLF model in Fig. 5(d) appears to be a blend of Fig. 5(b) and Fig. 5(c). The non-isothermal flows are further entrained toward the direction of the plate movement due to the viscosity increase toward the plate.

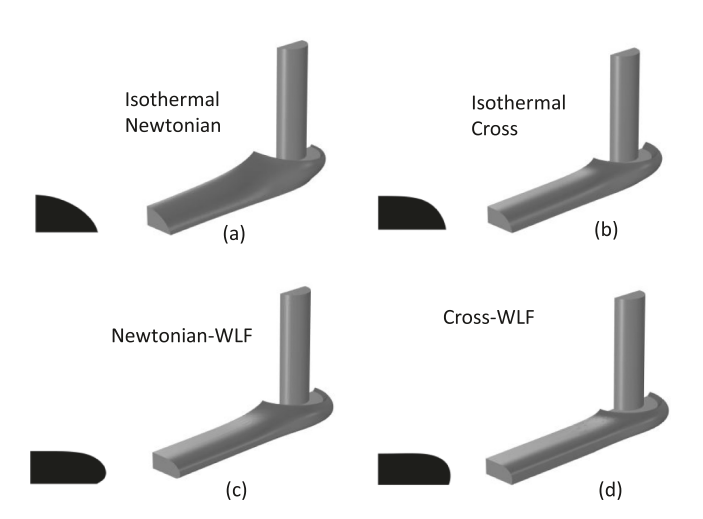


**Fig. 5.** Comparison of printing flows at 0.3 s together with the downstream cross-sections by (a) Newtonian,  $\eta_N$ , (b) isothermal Cross,  $\eta(\dot{\gamma},T_e)$ , (c) non-isothermal Newtonian-WLF,  $\eta(S/H,T)$ , and (d) Cross-WLF models.

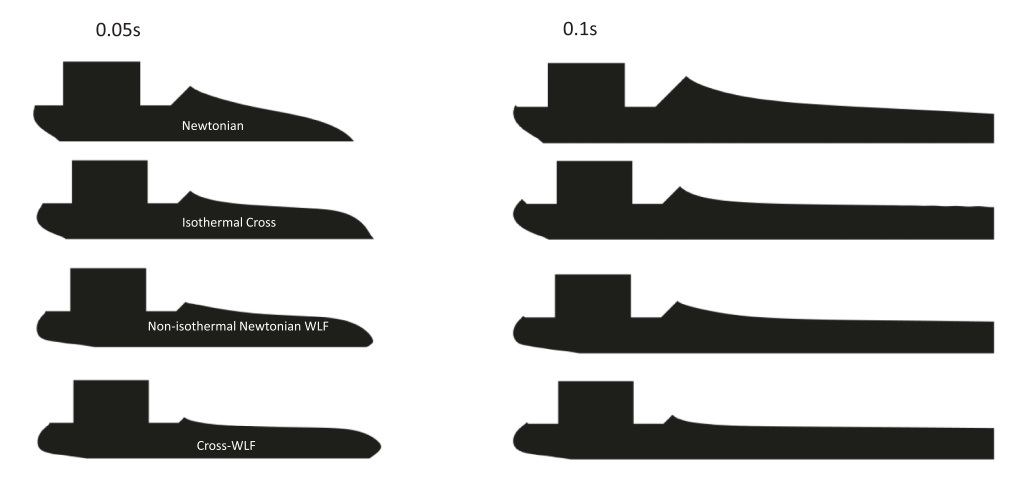


Fig. 6. Comparison of side views at 0.05 s and 0.1 s together by Newtonian, isothermal Cross, non-isothermal Newtonian-WLF and Cross-WLF models. Nozzle region is cropped out above z = 0.3 mm.

It is noted that the leading free boundaries (left of the nozzle centerline in Fig. 6) and the contact points with the substrate are differently formed for all the cases. In the non-isothermal cases, the shape of the upstream free boundary with the air is recessed toward the nozzle exit. To summarize the behavior of the trailing free boundaries (right of the nozzle center-line), the Newtonian models suggest a predominance of Couette flow that result in the trailing free boundary roughly parallel with the leading free boundary. For the non-isothermal flow models, traces of pressure-driven flows appear on the right boundary. Perhaps most importantly, the models suggest that the final thicknesses and widths of the printed road are significantly dependent on the material constitutive model. These results are important in that the shape of the printed road and related process states directly determine the intimate contact area and resulting printed part properties. Thus, in the remainder of this work unless otherwise specified, the Cross-WLF model is adopted to capture both the non-isothermal and non-Newtonian material viscosity behavior.

#### 3.4. Flow development and velocity field

Let us investigate how the printing flow develops along with time. Fig. 7 shows rendered views of the developing flow from 0.005 s. Up to

0.01 s the extruded flow expands spherically. Starting at 0.01 s, upon the flow front impacting the substrate, the flow becomes predominantly radial as a pressure-driven flow with a mostly symmetric velocity field about z equaling H/2. These presented results are similar to those found in the previous works [8,9] and can provide accurate information about the free boundary near the nozzle exit.

The velocity field is another topic of interest. Fig. 8 shows the stream tubes at 0.025 s. The flow from the nozzle impinges onto the substrate and tries to form a stagnation point where the radial flow of the extrudate out of the nozzle orifice matches the transverse velocity of the build plate. Moreover, the directional change around the stagnation point is the most pronounced flow phenomenon here. After the flow bends, the flow is driven not only by the build plate but also by the pressure. It can be seen that the paths toward the printing direction are varied and some stream tubes form a long way via the leading edge posing a steep angle of direction change. This redirection causes a large deformation of the fluid elements in a short period, which suggests a large  $\dot{\gamma}$  to be expected there.

# 3.5. Strain rate and Viscosity

The change in velocity streams observed in Fig. 8 can cause a high

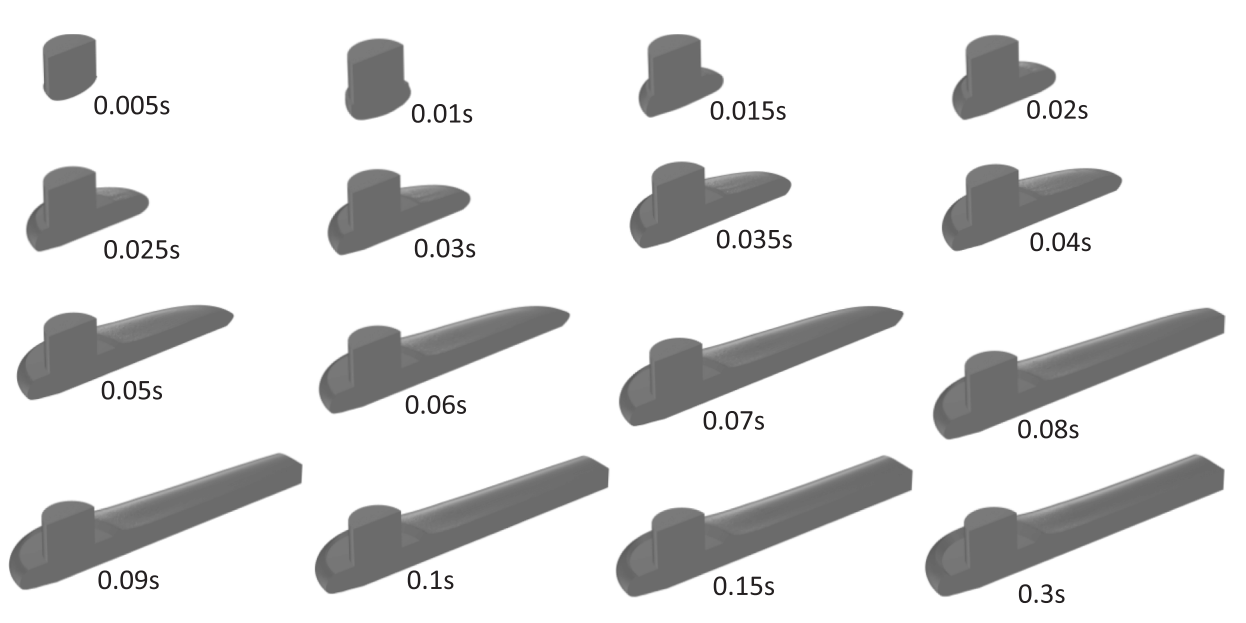
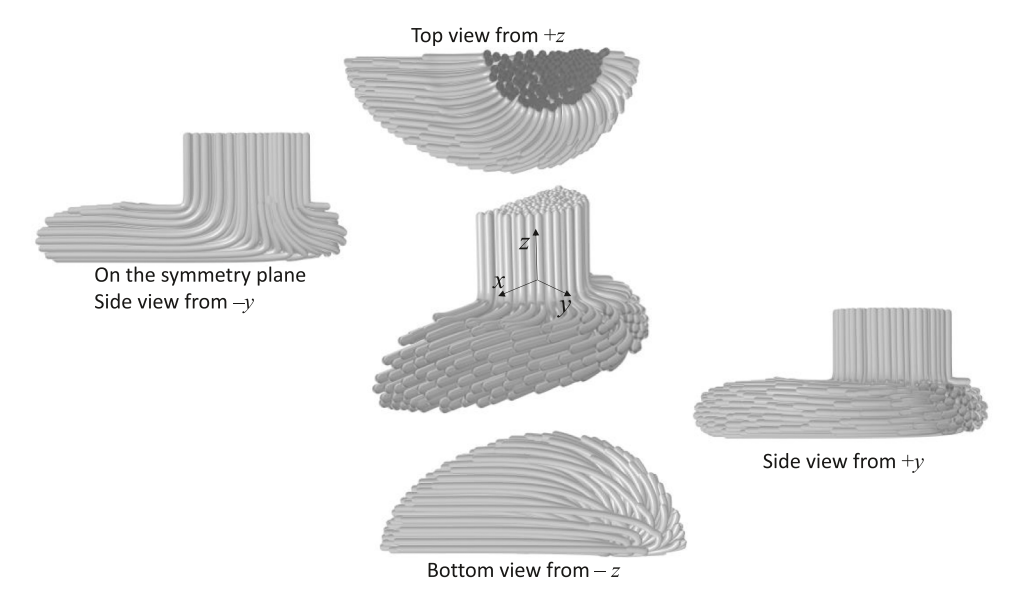


Fig. 7. Rendered view of flow development by Cross-WLF model from 0.005 s to 0.3 s. Nozzle region is cropped out above z = 0.4 mm.



**Fig. 8.** Stream tubes at t = 0.025 s. Nozzle region is cropped above z = 0.3 mm.

strain rate whereby the local strains, stresses, and temperatures are likely to play a significant role in the initial contact with the substrate and subsequent healing dynamics. Fig. 9 shows  $\dot{\gamma}$  according to the non-isothermal Cross model at t=0.5 s when the flow is fully developed. A slanted regime of high  $\dot{\gamma}$  is observed under the nozzle exit with  $\dot{\gamma}$  on the order of  $700~\text{s}^{-1}$ . The highest values of  $\dot{\gamma}$  are observed at the forward interface between the extruded melt and the moving substrate. The reason is that the melt front is expanding radially outward from the nozzle while at the same time the substrate is translating in a direction opposite the flow. Accordingly, the values of  $\dot{\gamma}$  on the leading surface of the substrate are on the order of  $1000~\text{s}^{-1}$ . For reference, the apparent shear rate for uniform flow between a fixed and moving plate would be

$$\dot{\gamma}_a = S_0/H = 41.7 \text{mm/s}/0.25 \text{mm} = 167 \text{s}^{-1}$$
.

Fig. 10 shows the non-isothermal viscosities for  $\dot{\gamma}$  of Fig. 9. The non-isothermal simulation shows a thick, highly viscous layer in the deposited road just opposite and downstream the nozzle corresponding to the location of the stagnation point. The reason is that the velocity of the expanding flow out of the nozzle closely matches the relative print speed of the substrate such that the values of high  $\dot{\gamma}$  approach zero and cooling quickly begins. The viscosity difference renders a pressure-driven flow through the surrounding lower viscosity regions. Consequently, under the right side of the nozzle bottom  $(+R_i < x < +R_o)$ , the region of high  $\dot{\gamma}$  in Fig. 10 surrounds a region of low  $\dot{\gamma}$  as in a slit flow. The viscosity of the downstream melt quickly rises as heat is conducted from the extrudate

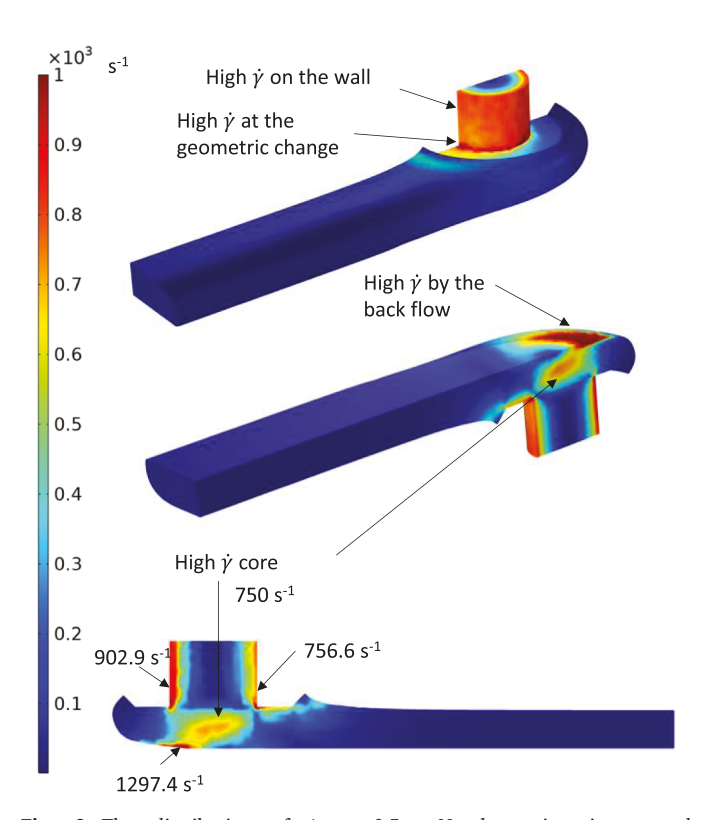


**Fig. 9.** The distribution of  $\dot{\gamma}$  at 0.5 s. Nozzle region is cropped above z=0.4 mm.

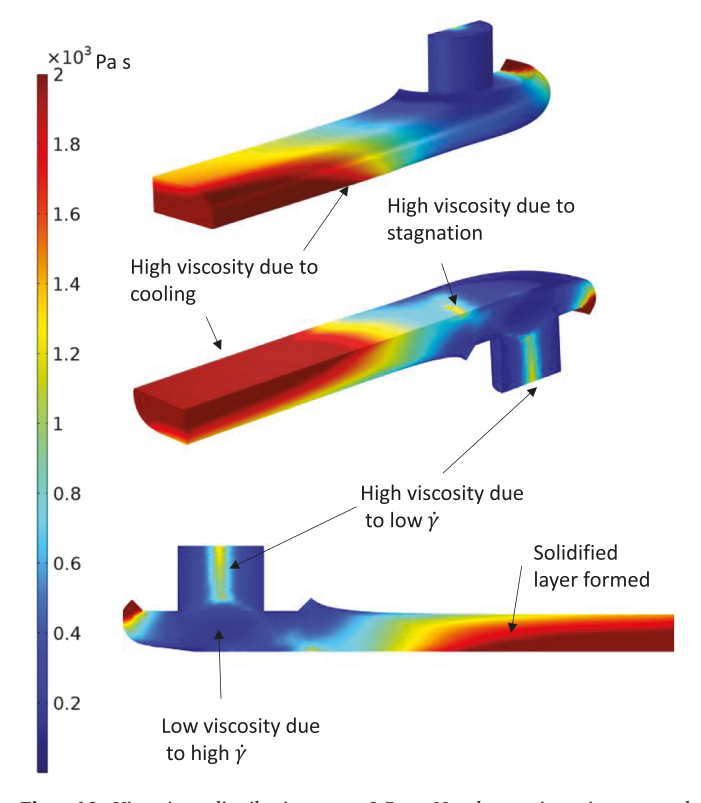


**Fig. 10.** Viscosity distribution at 0.5 s. Nozzle region is cropped above z=0.4 mm.

to the substrate even with a relatively low value of h modeled as 100 W/  $\rm m^2 K$ 

# 3.6. Contact area and thermal footprint

In this section, the shape of the contact area between the extruded road and the substrate as well as the resulting thermal footprint are investigated for varying heat transfer coefficients. Fig. 11 shows the contact area and thermal footprints from 0.02 s to 0.045 s for h equal to 0 (adiabatic case) as well as geometrically increasing values from 100 to  $1600 \text{ W/m}^2\text{K}$ . In the adiabatic case, there are slight temperature

gradients due to shear heating (see Supplemental Fig. S9) but the temperature appears constant given the broad contour scaling of Fig. 11. As the TCC, h, increases, the TCR decreases between the deposited road and the substrate. According to the theory of the TCR, the rate of heat conduction depends on the engaging materials, surface roughness and the interfacial pressure. As mentioned earlier, the interfacial pressure is quite low in comparison with molding processes. As a result, a relatively low value of h around  $100 \text{ W/m}^2\text{K}$  seems a reasonable choice based on the authors' experimental and simulation prior works. Unfortunately, it should be noted that experimental characterization is not available at this time and is suggested as future work. Regardless, the effects of h are

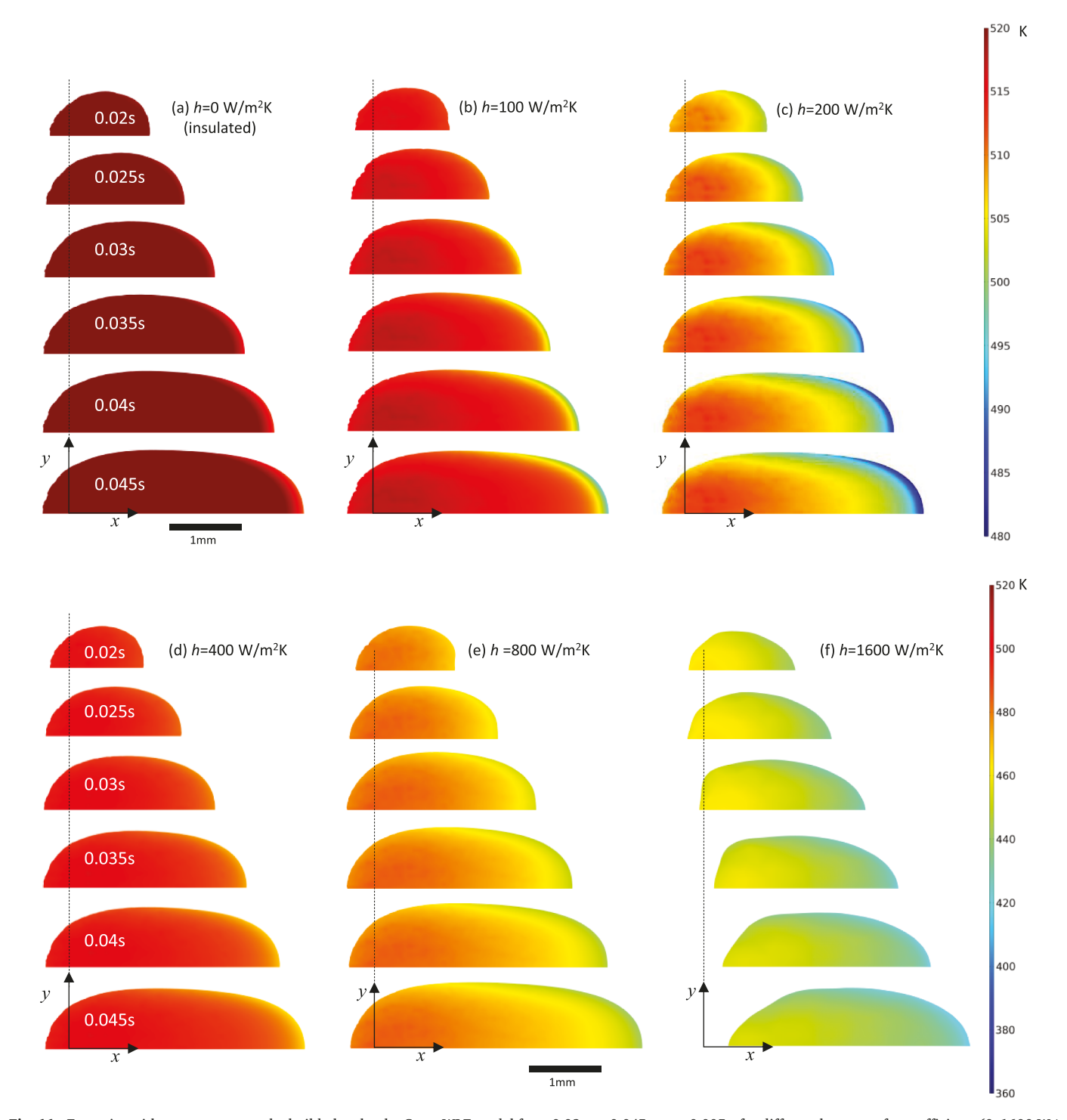


Fig. 11. Footprint with temperature on the build plate by the Cross-WLF model from 0.02 s to 0.045 s step 0.005 s for different heat transfer coefficients (0–1600 W/m<sup>2</sup>K). Note that the color map ranges from 480 K to 520 K for (a-c) and from 360 K to 520 K for (d-f).

investigated to understand the implication of the TCR in this process.

At lower values of h equal to 0, 100, and 200 W/m²K, the shapes of the contact areas appear identical. These results suggest that the extruded polymer remains molten and flowing in the vicinity of the nozzle, such that an outward radial flow is maintained with  ${\bf u}$  and  $\dot{\gamma}$  distributions as previously described. The temperatures of the footprints do vary significantly with these lower values of h. For h equal to 100 W/m²K, the temperature of the deposited road at the interface with the substrate decreases from 520 K to 515 K opposite the nozzle and then to 500 K downstream the nozzle at 0.045 s. For h equal to 200 W/m²K, the temperature of the deposited road at the interface with the substrate decreases from 520 K to 510 K opposite the nozzle and then to 480 K downstream the nozzle at 0.045 s

Now, let us investigate if h is further increased to 400, 800, and  $1600 \text{ W/m}^2\text{K}$ . For 400 and  $800 \text{ W/m}^2\text{K}$ , the shapes of the contact area look similar as for the isothermal case again indicating a radial flow out of the nozzle. However, for  $1600 \text{ W/m}^2\text{K}$ , the leading edge of the contact area after 0.02 s noticeably shifts downstream. The reason is that the cooling of the extruded melt with increased h causes the development of a viscous flow front that impedes the radial flow of the material in the vicinity of the nozzle. A greater proportion of the flow is redirected above the contact plane with the substrate causing the width of the footprint near the nozzle to narrow. This narrowed and shifted footprint below the nozzle exit will eventually cause detachment of the extrudate from the nozzle and suggests the existence of process constraints related to the thermal properties of the material being processed.

The temperature of the interface between the deposited road and the substrate also varies significantly with h. The simulation predicts an interface temperature opposite the nozzle decreasing from 520 K (isothermal) to 500, 470, and 440 K for respective heat transfer coefficients of 400, 800, and 1600 W/m²K. The downstream temperatures after 0.045 s are further affected with predicted interface temperatures of 480, 440, and 420 K respectively. The temperature decrease in Fig. 11 (f) is large enough to cause a significant increase in viscosity resulting in the change of the footprint shape. Accordingly, these thermo-rheological phenomena have a profound effect on the shape of the initial contact area, temperature history, weld healing, and ultimate part properties. These temperature transients can be used with weld healing models [34] to provide higher fidelity strength predictions than currently reported in the literature which do not model the 3D temperature field as accurately.

#### 3.7. Pressure development

It is important to investigate the pressure development as the contact

pressure between the deposited road and substrate has a great effect on interlayer adhesion since fusion bonding requires compressive stress at the interface [15]. Fig. 12 shows the pressure distribution at the center-line of the deposited road at different times as the flow field fully develops for  $h = 100 \text{ W/m}^2\text{K}$ . The melt pressure is initially zero with a nearly isothermal melt. As the printing process continues, heat conduction causes the deposited material to slightly cool including in the vicinity of the nozzle, thereby causing the melt pressure distribution below the nozzle to increase and equilibrate around 400 kPa. The pressure distribution is not symmetric with respect to the nozzle center-line. Rather, the pressure peaks occur with a slight shift in the positive x-direction (downstream). This shift in the pressure peak is associated with the higher strain rates leading the deposition of the material as previously described and the required redirection of the melt around the downstream stagnation point. Furthermore, a negative pressure is observed downstream the exterior nozzle face (x > 0.55 mm) associated with the free expansion of the melt as the extruded material climbs and releases from the exterior nozzle face.

The pressure distributions are also influenced by the thermal conditions. Fig. 13 shows pressure profiles along the center-line and substrate for various models and heat transfer coefficients at t = 0.045 s. The results indicate that there is a positive contact pressure on the order of 100 kPa related to the radial melt flow out of the nozzle orifice; this contact pressure would substantially increase as the layer thickness H is reduced from 0.25 mm and can play a significant role in initial contact and subsequent healing. The pressures tend to be highest directly below the nozzle orifice where the melt is constrained and must flow outward radially, and then quickly decays as the melt flows beyond the confines of the nozzle's exterior faces. The isothermal Cross model (h = 0 W/m<sup>2</sup>K) has the lowest pressures given the uniform melt temperatures associated with no cooling. As the heat transfer coefficient increases, the reduced melt temperatures drive higher melt viscosities and resultant pressures. The Newtonian model also provides relatively higher pressures since the shear thinning of the viscosity is not modeled. The pressures are observed to vary slightly from the center-line (z = -H/2) to the substrate (z = -H). Generally, one would expect highest pressures at the center of the nozzle orifice (z = H/2) with pressures decaying radially therefrom. However, the results suggest that the pressures at the substrate (z = -H) are slightly higher than at the center-line. Neglecting the momentum, the force balance between the nozzle exit and the projected area on the substrate implies that the pressures be equal at the nozzle orifice and substrate. However, the viscous dissipation along the streamline causes a pressure decrease. As a result, the pressure decreases from the nozzle exit and then increases back toward the substrate.

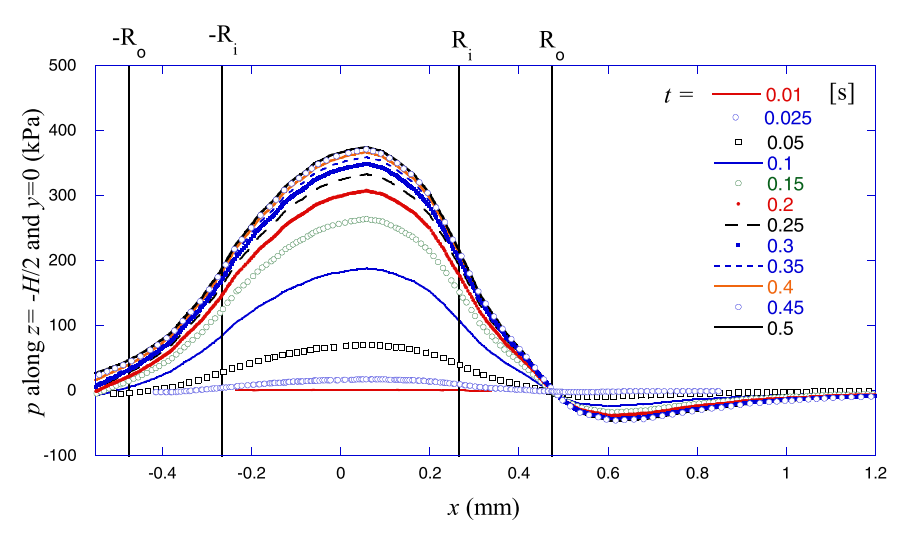


**Fig. 12.** Pressure along z = -H/2 and y = 0 for different times by  $h = 100 \text{ W/m}^2\text{K}$ .

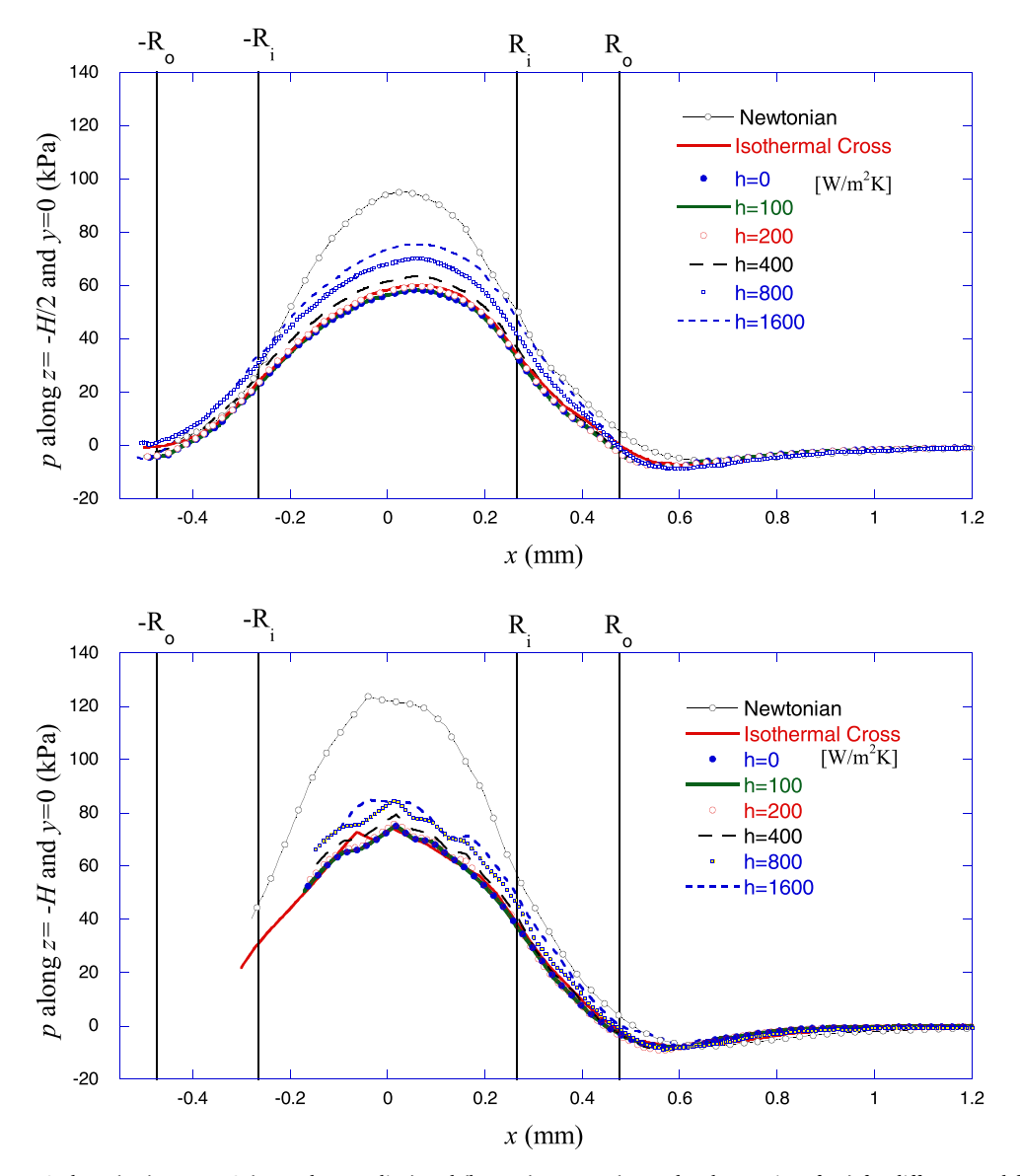


Fig. 13. Pressure for y = 0 along (top) z = -H/2 (at road center-line) and (bottom), z = -H (at road: substrate interface) for different models at t = 0.045 s. The results are obtained with the Cross-WLF model unless otherwise indicated.

# 3.8. Effects of Q and S

The flow rate and the speed of the build plate are process variables critical to the printing of the road, which are interrelated with each other [42]. Fig. 14 shows how changing Q affects the dimension and shape of the printed road as well as the pressure distributions. Generally, increased Q causes greater melt pressures in and below the nozzle, through the pressure distribution decays as the melt clears the exterior nozzle faces. Of course, higher flow rates at the same print speed  $S_0$  will drive larger road cross-sections. Interestingly, the widths and heights of the printed roads are not directly proportional to Q due to the lateral flow. Recalling that the nozzle height *H* is set to 0.25 mm, the indicated resultant road heights are 87.6%, 84.8%, 80.8%, and 68.8% of H. Calculating the measured full road width to the measured road height ratio in Fig. 14, one finds these results provide width; height ratios of 4.25, 3.74, 2.94, and 2.22 for flow rates of 10.4, 7.8, 5.2, and 2.6 mm<sup>3</sup>/s. Furthermore, the ratio of the measured full road width to the nominal road width, W, are calculated as 0.93, 1.06, 1.19, 1.53 for the same flow rates in that order. These results suggest that lower flow rates are likely detrimental to contact area and part strength as the top surface of the cross-section quickly rolls off. The higher contact pressure associated

with higher flow rates is also aid in weld healing.

Now, let us check the effect of S on the printed roads. Fig. 15 shows the printing flows at increased print speeds S. As can be predicted, an increase in S here causes an effect similar to a decrease in Q in Fig. 14. An increased S results in a deflated leading surface and a more retracted contact point on the substrate. The cross-section also changes per Eq. (13) with a greater reduction in road width than road height as shown in Supplemental Fig. S7. Surprisingly, the values of  $\dot{\gamma}$  are not significantly influenced by the print speed except in the vicinity of the build plate. Accordingly, these results indicate that the volumetric flow rate is the primary determinant of the shear rate in the vicinity of the nozzle with the maximum shear rate occurring near the stagnation point on the substrate rather than on the nozzle wall. The maximum  $\dot{\gamma}$  on the bottom of the nozzle wall is believed to be the effect of the nozzle wall flow having extended outward.

# 3.9. Comparison with experimental pressure

As elaborated in [14,15], the contact pressure,  $p_{\text{contact}}$ , can be experimentally acquired by the difference between the pressure while normal printing flow,  $p_{\text{print}}$ , and the one while the open purge flow,

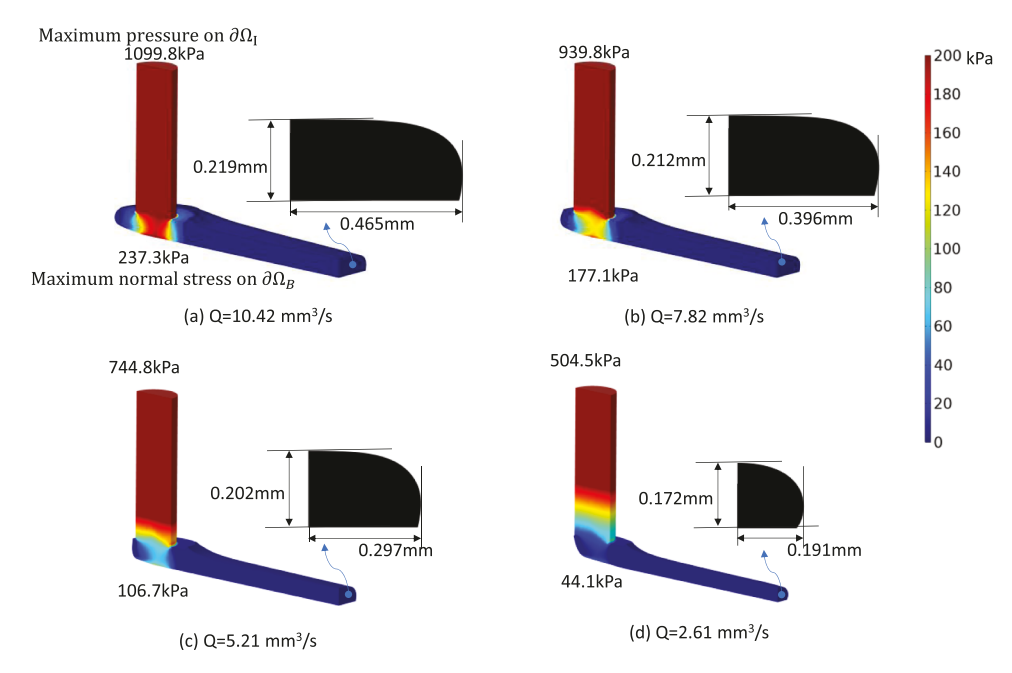


Fig. 14. Effects of flow rate at 0.1 s together with the inlet pressure and the maximum normal stress on  $\partial\Omega_B$ .

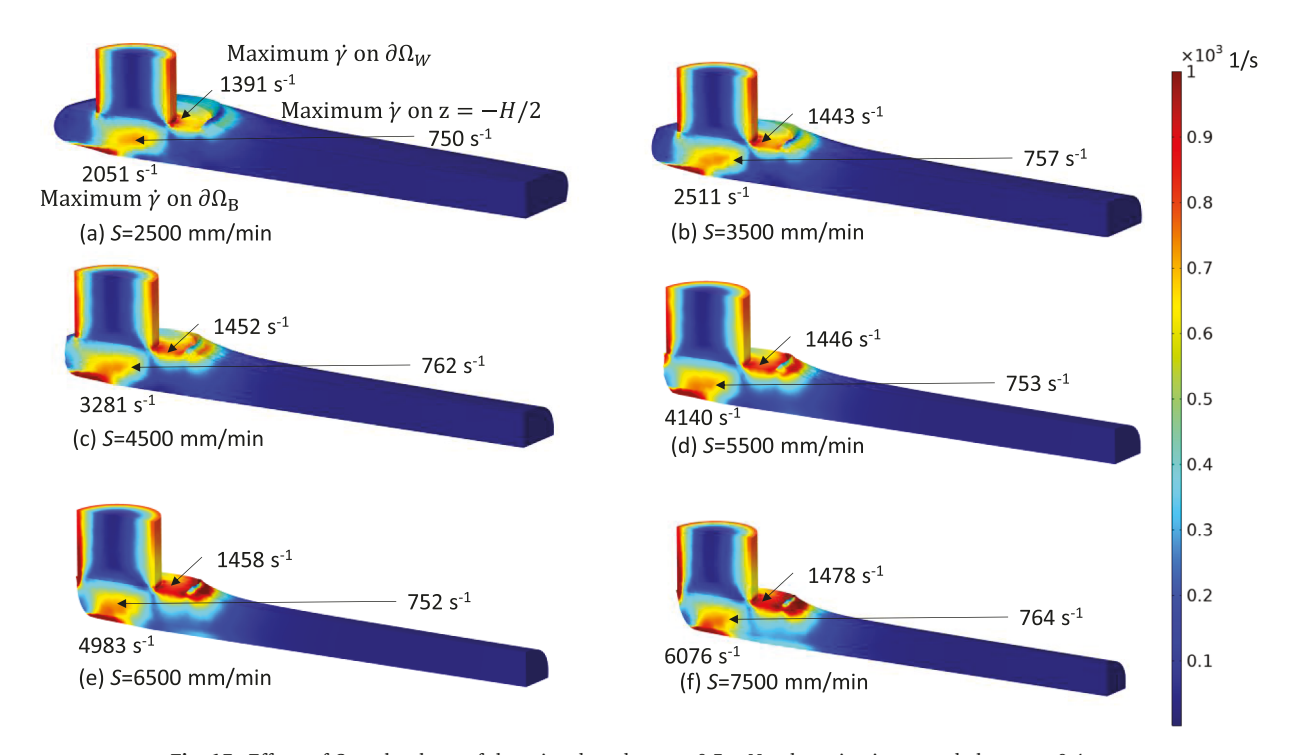


Fig. 15. Effects of S on the shape of the printed roads at t = 0.5 s. Nozzle region is cropped above z = 0.4 mm.

 $p_{\rm open}$  as conceptualized in Supplemental Fig. S8. Both  $p_{\rm print}$  and  $p_{\rm open}$  are evaluated as the integrated average across the orifice boundary  $\partial\Omega_{\rm I}$  for a simulated fully developed flow with t = 1 s. Since both the pressures,  $p_{print}$  and  $P_{open}$ , change over time, the contact pressure is evaluated when the flow is sufficiently developed. The numerically predicted contact pressures will be compared with experimental observations denoted as DOE1( $Q=5.21~{\rm mm}^3/{\rm s}$ ), DOE2 ( $Q=6.77~{\rm mm}^3/{\rm s}$ ) and DOE3 ( $Q=3.65~{\rm mm}^3/{\rm s}$ ) in [15]. Fig. 16(a) shows those three pressures together for all three DOE cases to be compared. Based on the numerically simulated pressures at 1 s, the contact pressures are evaluated and compared with the experimental data. As shown in Fig. 16(b), the numerical contact pressures agree well with the experimental data. Note that DOE16 in the

figure is a replicated experiment of DOE1 as indicated in [15]. These results demonstrate the validity of the presented numerical method.

#### 4. Discussion

To obtain the result for DOE1 (single case for  $Q=5.21~\mathrm{mm}^{3/s}$ ) in Figs. 16, 11.3 GB of memory and approximately 31 h of CPU (AMD Ryzen 3955WX) time have been consumed. The convergence was not monotonic since the level of nonlinearity was quite high. Moreover, as this work does not involve any solidification model or no flow temperature (NFT) [43], the flow slowly continues even at a high viscosity. Since this demands high computational load, incorporation of

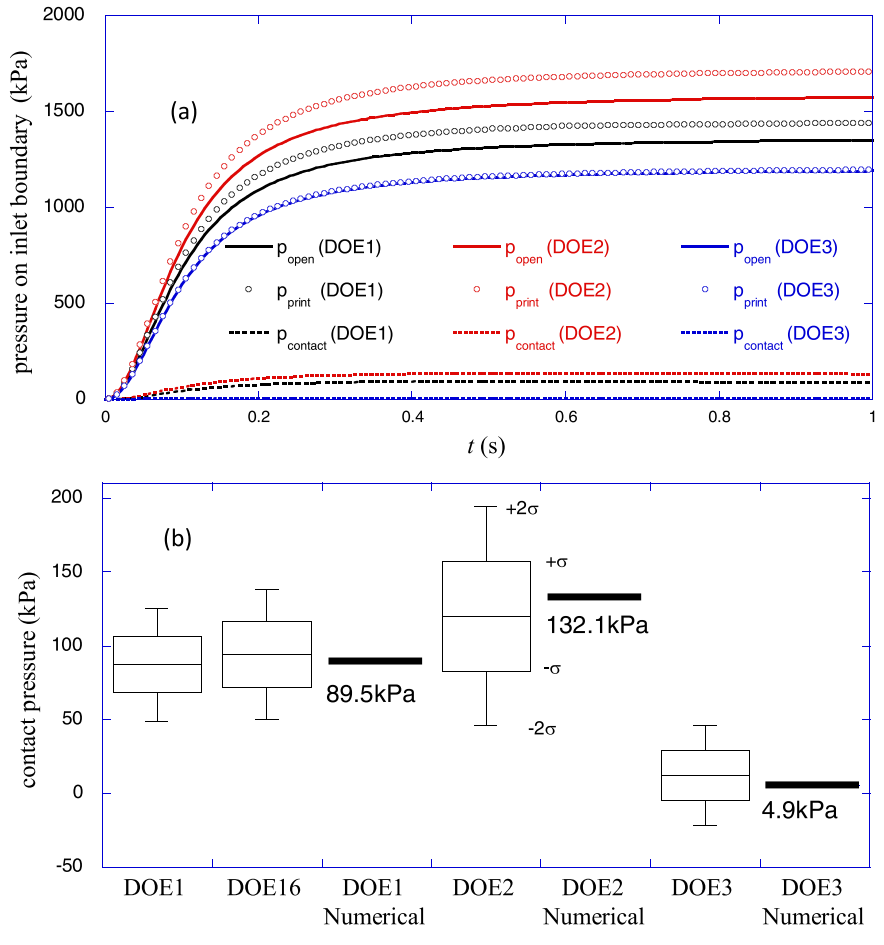


**Fig. 16.** (a) Numerically evaluated contact pressure and (b) comparison with the experimentally measured contact pressures. DOE1, DOE2 and DOE3 corresponds to *Q* of 5.21, 6.77 and 3.65 mm<sup>3</sup>/s, respectively. DOE16 is replicated experiment of DOE1 [15].

solidification model would help shorten the computational time. The computational domain in Fig. 3 with half symmetry can also be replaced by the full model of the printed road. In this case,  $\partial\Omega_S$  disappears and the computational domain is doubled. If calculated in this way, the required memory was increased to 26.5 GB but the CPU time was reduced to 19 h. The temperature field by this approach is shown in Fig. 17. The reason for CPU time saving is presumed to be that imposition of the Neumann condition on the plane of symmetry together with the determination of the interface,  $\partial\Omega_A$ , on  $\partial\Omega_S$ . It has been observed that the level set equation requires very long iterations for the smaller  $\gamma$ . The full model requires a smaller number of iterations for the level set equation with the same  $\gamma$ .

As aforementioned, the mesh convergence has been checked to verify that there is no uncertainty associated with the numerical discretization error. In addition, to examine the validity of the model, the result has been compared with the experimental data in the previous section. Here, to check for errors due to uncertainty with respect values on the input variables, sensitivity analyses has been performed for the DOE1 by varying the simulation parameters S,  $T_m$  (K), Q,  $T_{plate}$  (K) and  $D_1$  by 1% each. For the five varied cases, the maximum change in the peak extrudate pressure was found to be 1.78% relative to the nozzle exit pressure. The simulations with the isothermal Newtonian, isothermal Cross and Newtonian-WLF gave similar results. Thus, the proposed method is overall stable and reliable as a numerical tool.

#### 5. Conclusion

This work has presented 3D simulation of material extrusion additive manufacturing processes with a generalized Newtonian fluid under non-

isothermal conditions using the Cross-WLF rheological model. The evolution scheme for the viscosity has been proposed and implemented using acceleration models for the build plate and the filament feeding. Prior work has found that finite element modeling with a generalized Newtonian model can provide reasonable prediction of the melt extrusion in the vicinity of the nozzle. However, our results have shown that the non-isothermal model with shear thinning is required and the thermal gradients within the printed road play a critical role in the ultimate shape of the road cross-section. Especially, it has been visualized that the thermal contact resistance affects the shape of the contact area and subsequent thermal footprint on the substrate with ramifications on the pressure field and subsequent weld healing. Moreover, the thermorheological conditions change the flow front shapes on the free boundaries through the movement of the stagnation point opposite the nozzle and redirection of the leading flow front.

The simulated pressure distributions in this work have been compared with previous experimental results estimating the contact pressure. Both the contact pressures are in good agreement with each other supporting the validity of the described numerical method. As the developed method operates in a reliable way, it will be able to help the analysis and design of a fused filament fabrication process. While the presented simulation can well describe the flow in the vicinity of the nozzle, further modeling including melt compressibility and the normal stress between the nozzle and substrate are recommended for future studies to provide high fidelity prediction of the final road dimensions and strength.

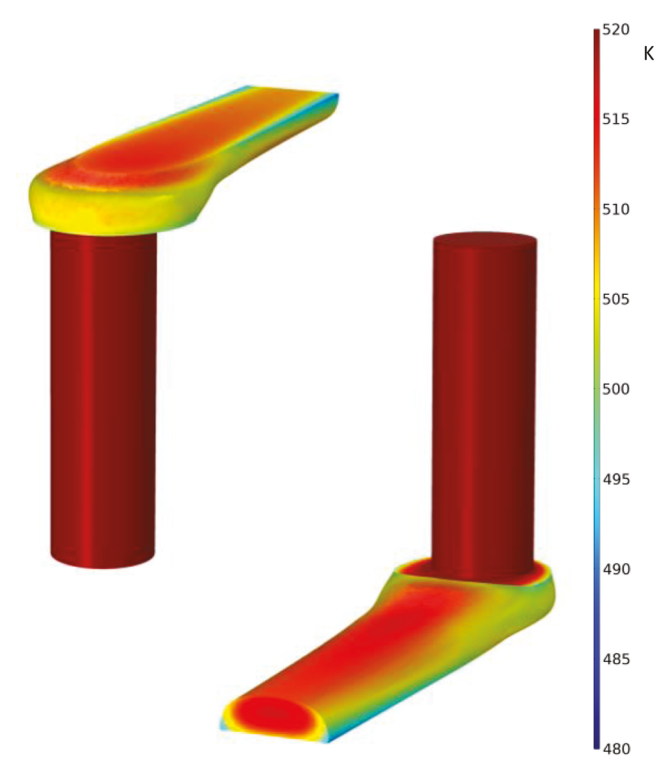


Fig. 17. Calculation of temperature for  $Q = 5.21 \text{ mm}^3/\text{s}$  at 0.1 s without the symmetry condition.

#### **Funding**

This work was supported by the National Research Foundation of Korea (NRF) grant funded by the Republic of Korea government (MSIT) (NRF-2018R1A5A1024127 and NRF-2020R1I1A2065650). Portions of this work are also based upon work supported by the National Science Foundation under Grant (USA) No. #1914651. Any opinions, findings, and conclusions or recommendations expressed in this material are those of the authors and do not necessarily reflect the views of the National Science Foundation.

# CRediT authorship contribution statement

**Sun Kyoung Kim:** Conceptualization, Formal analysis, Methodology, Software, Writing – original draft. **David O. Kazmer:** Conceptualization, Formal analysis, Methodology, Validation, Writing – review & editing.

# **Supplemental Materials**

The supplemental materials include nine additional figures related to the start-up acceleration and velocity and pressure fields, thermal footprints and viscosity fields for additional heat transfer coefficient values, and additional cross-sections shown the geometry, pressure, and temperature.

### **Declaration of Competing Interest**

The authors declare that they have no known competing financial interests or personal relationships that could have appeared to influence the work reported in this paper.

# Appendix A. Supporting information

Supplementary data associated with this article can be found in the

online version at doi:10.1016/j.addma.2022.102833.

#### References

- I. Gibson, D. Rosen, B. Stucker, Addit. Manuf. Technologies: 3D Printing, Rapid Prototyping, and Direct Digital Manufacturing, second ed., Springer-Verlag., New York, 2015.
- [2] B.N. Turner, R. Strong, S.A. Gold, A review of melt extrusion additive manufacturing processes: I. Process design and modeling, Rapid Prototyp. J. 20 (2014) 192–204.
- [3] H. Bikas, P. Stavropoulos, G. Chryssolouris, Additive manufacturing methods and modelling approaches: A critical review, Int. J. Adv. Manuf. Technol. 83 (2016) 389–405
- [4] A. Bellini, Fused Deposition of Ceramics: A Comprehensive Experimental, Analytical and Computational Study of Material Behavior, Fabrication Process and Equipment Design. Ph.D. Thesis, Drexel University, Philadelphia, 2002.
- [5] H.S. Ramanath, C.K. Chua, K.F. Leong, K.D. Shah, Melt flow behavior of polycaprolactone in fused deposition modelling, J. Mater. Sci. Mater. Med. 19 (7) (2008) 2541–2550.
- [6] H. Xia, J. Lu, S. Dabiri, G. Tryggvason, Fully resolved numerical simulations of fused deposition modeling. Part I: fluid flow, Rapid Prototyp. J. 24 (2) (2018) 463–476, https://doi.org/10.1108/RPJ-12-2016-02172018.
- [7] H. Xia, J. Lu, G. Tryggvason, A numerical study of the effect of viscoelastic stresses in fused filament fabrication, Comput. Methods Appl. Mech. Eng. 346 (2019) 242–259, https://doi.org/10.1016/j.cma.2018.11.031.
- [8] R. Comminal, M.P. Serdeczny, D.B. Pedersen, J. Spangenberg, Numerical modeling of the strand deposition flow in extrusion-based additive manufacturing, Addit. Manuf. 20 (2018) 68–76. https://doi.org/10.1016/j.addma.2017.12.013.
- [9] J.-F. Agassant, F. Pigeonneau, L. Sardo, M. Vincent, Flow analysis of the polymer spreading during extrusion additive manufacturing, Addit. Manuf. 29 (2019), 100794. https://doi.org/10.1016/j.addma.2019.100794.
- [10] B. Behdani, M. Senter, L. Mason, M. Leu, J. Park, Numerical study on the temperature-dependent viscosity effect on the strand shape in extrusion-based additive manufacturing, J. Manuf. Mater. Process 4 (2020) 46, https://doi.org/ 10.3390/jmmp4020046.
- [11] A. Gosset, D. Barreiro-Villaverde, J.C. Becerra Permuy, M. Lema, A. Ares-Pernas, M.J. Abad López, Experimental and numerical investigation of the extrusion and deposition process of a poly(lactic acid) strand with fused deposition modeling, Polymers 12 (2020) 2885.
- [12] D.D. Phan, J.S. Horner, Z.R. Swain, A.N. Beris, M.E. Mackay, Computational fluid dynamics simulation of the melting process in the fused filament fabrication additive manufacturing technique, Addit. Manuf. 33 (2020), 101161.
- [13] T.J. Coogan, D.O. Kazmer, In-line rheological monitoring of fused deposition modeling, J. Rheol. 63 (2019) 141–156, https://doi.org/10.1122/1.50546482020.
- [14] S.K. Kim, D.O. Kazmer, A.R. Colon, T.J. Coogan, A.M. Peterson, Non-Newtonian modeling of contact pressure in fused filament fabrication, J. Rheol. 65 (2021) 27–42, https://doi.org/10.1122/8.0000052.
- [15] T.J. Coogan, D.O. Kazmer, Modeling of interlayer contact and contact pressure during fused filament fabrication, J. Rheol. 63 (4) (2019) 655–672.
- [16] J. Liu, K.L. Anderson, N. Sridhar, Direct Simulation of Polymer Fused Deposition Modeling (FDM) — An implementation of the multi-phase viscoelastic solver in OpenFOAM, Int. J. Comput. Methods 17 (2020), 1844002.
- [17] M.E. Mackay, The importance of rheological behavior in the additive manufacturing technique material extrusion, J. Rheol. 62 (2018) 1549.
- [18] R.B. Comminal, J.H. Hattel, J. Spangenberg, Numerical simulations of planar extrusion and fused filament fabrication of non-newtonian fluids. nordic rheology society, Annu. Trans. 25 (2017) 263–270.
- [19] T. Osswald, J. Tim, J. Puentes, Kattinger, Fused filament fabrication melting model, Addit. Manuf. 22 (2018), https://doi.org/10.1016/j.addma.2018.04.030
- [20] M.M. Cross, Rheology of non-Newtonian fluids: A new flow equation for pseudoplastic systems, J. Colloid Interface Sci. 20 (1965) 417–437.
- [21] S.K. Kim, Collective viscosity model for shear thinning polymeric materials, Rheol. Acta 59 (1) (2020) 63–72.
- [22] M.L. Williams, R.F. Landel, J.D. Ferry, Temperature dependence of relaxation mechanisms in amorphous polymers and other glassforming liquids, J. Appl. Phys. 24 (1953) 911.
- [23] M. Sussman, P. Smereka, S. Osher, A. Level, Set approach for computing solutions to incompressible two-phase flow, J. Comput. Phys. 114 (1994) 146–159.
- [24] E. Olsson, G. Kreiss, A conservative level set method for two phase flow, J. Comput. Phys. 210 (2005) 225–246.
- [25] T.W.H. Sheu, C.H. Yu, P.H. Chiu, Development of level set method with good area preservation to predict interface in two-phase flows, Int. J. Numer. Methods Fluids 67 (2011) 109–134.
- [26] L. Ville, L. Silva, T. Coupez, Convected level set method for the numerical simulation of fluid buckling, Int. J. Numer. Meth. Fluids 66 (2011) 324–344.
- [27] Comsol 5.6 CFD Module User's Guide, Comsol AB, Stockholm, Sweden (2020).
- [28] C.V. Madhusudana, Thermal Contact Conductance, New York: Springer-Verlag, 1995.
- [29] C. Yu, J. Sunderland, C. Poli, Thermal contact resistance in injection molding, Polym. Eng. Sci. 30 (24) (1990) 1599–1606.
- [30] A. Bendada, A. Derdouri, M. Lamontagne, Y. Simard, Analysis of thermal contact resistance between polymer and mold in injection molding, Appl. Therm. Eng. 24 (14) (2004) 2029–2040.

- [31] F.B. Hsiao, D.B. Wang, C.P. Jen, Numerical investigation of thermal contact resistance between the mold and substrate on laser-assisted imprinting fabrication, Numer. Heat. Tr. A-Appl. 49 (7) (2006) 669–682.
- [32] E.M. Park, S.K. Kim, Effects of mold heat transfer coefficient on numerical simulation of injection molding, Trans. Korean Soc. Mech. Eng. B 43 (3) (2019) 201
- [33] J. Pedro, B. Ramôa, J.M. Nóbrega, C. Fernandes, Verification and validation of openInjMoldSim, an open-source solver to model the filling stage of thermoplastic injection molding, Fluids 5 (2) (2020) 84, https://doi.org/10.3390/fluids5020084.
- [34] T.J. Coogan, D.O. Kazmer, Prediction of interlayer strength in material extrusion, Addit. Manuf. 35 (2020), 101368.
- [35] Ansys Polyflow User's Guide, Ansys Inc, Canonsburg, PA, USA, 2013.
- [36] M.A. Alves, P.J. Oliveira, F.T. Pinho, Numerical methods for viscoelastic fluid flows, Annu. Rev. Fluid Mech. 53 (2021) 509–541.
- [37] E.J. Padilha Júnior, R.P. Soares, N.S.M. Cardozo, Analysis of equations of state for polymers, Polímeros 25 (3) (2015).

- [38] D.-N. Arnold, F. Brezzi, M. Fortin, A stable finite element for the Stoke equations, Calcolo vol. 21 (1984) 337–344.
- [39] G. Hauke, T.J.R. Hughes, A unified approach to compressible and incompressible flows, Comp. Meth. Appl. Mech. Eng. vol. 113 (1994) 389–395.
- [40] T.J.R. Hughes, M. Mallet, A new finite element formulation for computational fluid dynamics: III. The generalized streamline operator for multidimensional advectivediffusive system, Comp. Meth. Appl. Mech. Eng. vol. 58 (1986) 305–328.
- [41] G. Söderlind, L. Wang, Adaptive time-stepping and computational stability, J. Comp. Appl. Math. vol. 185 (2006) 225–243.
- [42] D.O. Kazmer, A.R. Colon, A.M. Peterson, S.K. Kim, Concurrent characterization of compressibility and viscosity in extrusion-based additive manufacturing of acrylonitrile butadiene styrene with fault diagnoses, Addit. Manuf. 46 (2021), 102106.
- [43] G. Mannella, V. La Carrubba, V. Brucato, W. Zoetelief, G. Haagh, No-flow temperature in injection molding simulation, J. Appl. Polym. Sci. 119 (2011) 3382–3392